Title
Structure of Laminar Sooting Inverse Diffusion Flames

Journal
Combustion and Flame, 149(4)

Author
Mikofski, Mark A

Publication Date
2007-06-01

DOI
http://dx.doi.org/10.1016/j.combustflame.2007.01.006

Peer reviewed

Title: Structure of Laminar Sooting Inverse Diffusion Flames

Authors: Mark A. Mikofski[1]
Timothy C. Williams[2]
Christopher R. Shaddix[2]
A. Carlos Fernandez-Pello[1]
Linda G. Blevins[2†]

Affiliations: [1]Microgravity Combustion Laboratory, University of California Berkeley, Berkeley, CA 94720
[2]Combustion Research Facility, Sandia National Laboratories, Livermore, CA 94550
[†]Current Address: Office of Basic Energy Sciences, U.S. Department of Energy, Germantown, MD 20874

Article Type: Full Length Article

Correspondence Address:
Linda G. Blevins
U.S. Department of Energy
Office of Basic Energy Sciences
Germantown, MD 20874
Tel. (301) 903-1293
Fax (301) 903-6594
linda.blevins@science.doe.gov

Keywords: inverse diffusion flame, laminar, OH, PAH, laser-induced fluorescence, soot, laser-induced incandescence

Abstract

Flame structure of laminar inverse diffusion flames (IDFs) was studied to gain insight into soot formation and growth in underventilated combustion. Both ethylene-air and methane-air IDFs were examined, fuel flow rates were kept constant for all flames of each fuel type, and air flow rates were varied to observe the effect on flame structure and soot formation. Planar laser-induced fluorescence of hydroxyl radicals (OH PLIF) and polycyclic aromatic hydrocarbons (PAH PLIF), planar laser-induced incandescence of soot (soot PLII), and thermocouple-determined gas temperatures were used to draw conclusions about flame structure and soot formation. Flickering, caused by buoyancy-induced vortices, was evident above and outside the flames. The distances between the OH, PAH and soot zones were similar in IDFs and normal diffusion flames (NDFs), but the locations of those zones were inverted in IDFs relative to NDFs. Peak OH PLIF coincided with peak temperature and marked the flame front. Soot appeared outside the flame front, corresponding to temperatures around the minimum soot formation temperature of 1300 K. PAH appeared outside the soot layer, with characteristic temperature depending on the wavelength detection band. PAH and soot began to appear at a constant axial position for each fuel, independent of the rate of air flow. PAH formation either preceded or coincided with soot formation, indicating that PAH are important components in soot formation. Soot growth continued for some time downstream of the flame, at temperatures below the inception temperature, probably through reaction with PAH.

Introduction

Soot and soot precursors, such as PAH, form during fuel-rich combustion. In the form of particulate matter, soot is a health concern and also a regulated pollutant that is receiving increased attention from governments due to studies that reveal that ultra-fine particles penetrate deep into the lungs [1,2]. Some potential soot precursors, such as some PAH, are also known carcinogens [3]. Furthermore, soot is an important factor in the rapid spread of accidental fires through radiant heat transfer [3-6].

Accurate soot formation models are needed to predict and control soot formation. Although such models have progressed significantly, soot inception and early soot growth are still not well understood [3,7-12]. Experimental results are needed to support the development of soot inception and growth models. Although there has been significant research on soot formation in laminar NDFs, research on soot formation in underventilated flames has been limited [13]. This paper aims to use IDFs to gain insight into soot inception and growth and to learn more about soot formation in underventilated fires.

In a co-flowing IDF, a central air jet is surrounded by a fuel jet [14]. This is the inverse of a co-flowing NDF, in which an air jet surrounds a central fuel jet. Since soot forms on the fuel side of diffusion flames [15,16], in IDFs, soot forms on the outside of the flame. Therefore, as in underventilated NDFs, soot escapes unoxidized from IDFs because soot never passes through the flame but instead moves outward to cooler regions of the fuel stream [8,17,18]. Therefore, IDFs have the potential to emit considerable quantities of soot similar to underventilated combustion [16,19-21].

The soot collected from IDFs is tar-like and has a high hydrogen content [22,23], and it has been found to be similar in chemical composition and morphology to soot collected from underventilated NDFs [24]. FT-IR and ^{1}H NMR spectroscopy of soot collected in an ethylene IDF show that low in the flame the soluble fraction of soot has an aliphatic chemical structure, which becomes progressively more aromatic at increasing height above the burner [25]. In addition, because IDF soot cools rapidly in the low temperature fuel stream and never passes through an oxidizing region, early soot inception and growth processes are isolated more in IDFs than in NDFs, allowing a systematic study of the early stages of soot formation [8,16,21,22]. Therefore, IDFs may provide useful insights into soot inception and growth and may be used as a tool to study soot formation in underventilated fires.

Compared to the vast amount of research on the structure of NDFs and counter-flow flames, there have been few studies on IDFs [14-18,21,26]. Flame structure of sooting IDFs has been reported in only a few papers. Kang *et al.* measured soot laser light scattering (LS) and PAH laser-induced fluorescence (LIF) in a nitrogen-diluted propane co-annular IDF with oxygen enrichment [15]. Lee *et al.* measured soot LS, PAH LIF in two bands, and OH LIF in C_2H_4 co-annular IDFs of varying dilution and flame temperature [26]. Shaddix *et al.* measured soot PLII, OH PLIF, and PAH PLIF in a methane-air IDF and an ethylene-air IDF on a co-flowing Wolfhard-Parker slot burner [18].

The objectives of this paper are (1) to examine the detailed structure of IDFs to gain insight into soot inception and early soot growth and (2) to study the effect of fuel structure and residence time on soot inception and early soot growth in IDFs. The flame

structure of co-annular IDFs of two different fuels, CH_4 and C_2H_4, is examined using OH PLIF, soot PLII, PAH PLIF, and temperature measurements. OH PLIF is used to determine the location of the reaction zone since OH exists on the air side of laminar diffusion flames very close to stoichiometric conditions and peak temperatures [18,26-28]. This is especially useful for IDFs since soot radiation masks the blue emission usually used to locate the reaction zone [24,29]. The air flow rate is varied to change flame height, so that the effect of residence time on soot and PAH formation can be investigated. This is the first study to examine this effect in IDFs. The detailed measurements reported in this paper provide a more complete understanding of IDF flame structure than was previously possible.

Experimental Methods

Apparatus

The co-annular burner used to support laminar IDFs in this study is similar to the one used by Blevins *et al.* [24] and was previously used in the flame height study of Mikofski *et al.* [29]. The burner consisted of three concentric tubes as shown in Figure 1. The tube edges were sharpened to reduce shear at the boundaries between flows. Air flowed through a 1-cm diameter central tube, which contained a screen to flatten the velocity profile. Fuel flowed in the annulus between a 3-cm diameter tube and the central air tube. The fuel annulus contained a honeycomb to smooth the flow. To prevent secondary flames from forming between the fuel and ambient air, nitrogen flowed through a second annulus formed between a 6.4-cm diameter outer tube and the 3-cm diameter tube. The nitrogen annulus contained screens and glass beads to straighten the

flow. The burner was attached to a translation stage that could be adjusted vertically with a precision of 0.5 mm. To reduce flame instabilities caused by room air currents, the burner was surrounded by a metal shield with openings to admit laser light and to provide optical access for a camera.

Table 1 lists the air and fuel flow rates for the CH_4 and C_2H_4 IDFs tested. Flame heights as a function of the rate of air flow for most of the flames in Table 1 have been previously published [29]. All of the flames tested were laminar, with Reynolds number less than 400, based on the cold flow velocities at the burner exit. All of the flames were also buoyant, with Froude numbers less than 0.5 based on the formula given in Ref. [30]:

$$Fr = \frac{\left(V_{air} Y_{air}\right)^2}{0.6 g L_f \left(T_f / T_0 - 1 \right)}, \tag{1}$$

in which V_{air} is the cold flow velocity of the air at the burner exit, Y_{air} is the stoichiometric mass fraction of air, g is the acceleration of gravity, L_f is the measured flame height, T_f is a characteristic flame temperature, and T_0 is ambient temperature (300 K). The characteristic flame temperature, T_f, used in equation 1 was 1500 K, as recommended by Turns [30]. Fuel, air and nitrogen were provided by calibrated mass flow controllers. Nitrogen flow was fixed at a rate of 30 standard liters per minute (slpm, where standard conditions are 293 K and 101 kPa). Fuel flow rates were held constant for each fuel type, while the rate of air flow was varied to change the flame height.

Laser Diagnostics

Laser and Camera Configurations

The laser and camera configuration in this study was the one used by Shaddix *et al.* [18]. Ultraviolet (UV) laser light at 283.57 nm was used to simultaneously excite planar OH and PAH fluorescence. OH radicals were excited by the laser light in the relatively temperature insensitive $Q_1(8)$ line of the (1,0) band of the $A^2\Sigma^+ - X^2\Pi_i$ electronic system and detected at 308.9 nm in the (0,0) band. The laser light was also used to excite PLII emission from soot particles. The laser light was provided by a dye laser pumped by a pulsed, frequency-doubled Nd:YAG laser. The laser was pulsed at 10 Hz, the pulse width was approximately 8 ns per pulse, and the energy per pulse was approximately 12 mJ. Cylindrical lenses were used to form a laser sheet that was 51 mm high and 250 μm wide. Therefore, the average laser fluence per pulse was 0.09 J/cm^2, and the mean laser flux was 10^7 W/cm^2. The laser sheet was aligned vertically with the central axis of the burner. By repositioning the burner relative to the laser sheet, measurements were made at two vertical locations, from 3 mm below to 48 mm above the burner exit, and from 23 mm to 74 mm above the burner exit.

A gated, intensified charge-coupled device (ICCD) camera with a 45-mm focal length, f/1.8 UV-enhanced lens was used to collect OH PLIF, PAH PLIF, and soot PLII at a rate of 2.5 frames per second for 40 seconds totaling 100 frames. The line of sight of the camera was oriented perpendicular to the direction of the laser sheet, and the image plane was centered on the vertical axis of the burner. The ICCD camera stored the output for each pixel as a 16-bit absolute intensity value. To minimize irising effects of the slow-gating ICCD camera, relatively long intensifier gate widths of 200 ns were used for

the fluorescence and incandescence measurements. Without filters, the ICCD camera detected wavelengths of light between 200 nm and 900 nm.

Visible color images of the flames were recorded with a CCD camera (Panasonic WV-CP454) with a 16-mm focal length, f/8 Cosmicar lens at a rate of 30 frames per second for 8 seconds totaling 240 frames. Visible color images were time-averaged using all 240 frames.

OH and PAH PLIF

Measurements of OH and PAH PLIF were taken with two different sets of optical filtering to attenuate laser light scattering, soot PLII, C_2 Swan band emission at 516.5 nm [31] and visible and infrared (IR) natural flame radiation. In one approach, a combination of a 295 nm long-pass filter and a UV-quality 450 nm short-pass filter was used. For brevity, this combination of filters will simply be referred to as the "450 nm short-pass filter" hereafter. In the other approach, a 340 nm (80 nm FWHM) band-pass filter was used to better balance PAH and OH PLIF signals. The use of the two different filter band-passes also permitted attempts to identify and locate different size aromatics, because larger aromatics have been shown to have a stronger red-shift to their broadband fluorescence spectrum when excited in the UV [32-34]. The 200-ns intensifier gate on the ICCD was opened 100 ns before the laser pulse to assure it was fully open prior to the laser firing. Both OH and PAH PLIF measurements were corrected for spatial variations in the laser beam profile by measuring Rayleigh scattering through room temperature air and then assuming a linear relation between measured PLIF and incident laser fluence. A graph of the beam profile is shown in Figure 2, in which the observed laser fluence is

normalized by the maximum laser fluence. Figure 2 indicates that the laser fluence was greatest near the base of the laser sheet, and decreased to 60% of the maximum laser fluence near the top of the laser sheet. Considering the laser beam correction and irising effects of the camera, the OH PLIF and PAH PLIF should be considered as qualitative measurements.

Soot PLII

Measurements of soot PLII were made with a 570 nm long-pass filter to eliminate 516.5 nm C_2 Swan band emission. The 200-ns intensifier gate on the ICCD was opened 100 ns after the laser pulse to attenuate PAH PLIF, which has a lifetime of approximately 10 to 100 ns [34,35]. Examination of PAH PLIF and soot PLII signals with the 570 nm long-pass filter showed that PAH PLIF accounted for less than 10% of the measured soot PLII signal. Images of flame luminosity were also captured with the 570 nm long-pass filter but with the laser off. These were subtracted from the corresponding soot PLII measurements to remove interference from natural flame radiation.

The Rayleigh scattering measurements were not used to correct the soot PLII. The relation between soot LII and laser fluence is complicated by many other factors including laser wavelength, laser spatial profile, soot absorption function, detection gating, detection wavelength, and detection geometry [36-38]. Experiments on the fluence dependence of soot LII show a rapid rise in soot LII until a critical fluence is reached, followed by a "plateau" region where the slope is significantly less, or, sometimes, by a decrease in LII signal with increasing fluence. The complicated dependence of soot LII on laser fluence may be explained by the competing effects of

probe volume expansion, increased soot heating and increased vaporization of soot particles. A critical laser fluence of 0.2 mJ/cm^2 has been reported using a 532 nm wavelength Nd:YAG laser [37,38]. Since soot absorption is approximately inversely proportional to wavelength, laser light at shorter wavelengths is absorbed more, and less fluence is needed to heat the soot particles [37]. Therefore, at a wavelength of 283 nm, the current fluence of 0.1 mJ/cm^2 is likely close to the critical fluence level.

The measured soot PLII was corrected for spatial variations in the beam profile and the irising effects of the slow-gating ICCD camera by applying a 5th-order polynomial correction function as a function of height in the image. The coefficients of the polynomial were obtained by minimizing the average error between corrected soot PLII measurements from all of the C_2H_4 IDFs in the image overlap region (from 23-48 mm above the burner) of the two vertical locations where measurements were taken. A comparison of the beam profile and the soot PLII soot correction function, shown in Figure 2, suggests that the high laser fluence near the bottom of the beam profile caused a large increase in soot PLII. Considering the UV wavelength excitation, long gate delay and gate width, and variations in soot primary particle size, the soot PLII signal should be considered qualitative.

Analysis of Laser Measurements

Measured signals were time averaged using all 100 frames recorded by the ICCD camera. Three millimeters of data were discarded from the top and bottom of the images to remove effects from laser attenuation around the top and bottom of the openings in the

metal shield surrounding the burner and from the irising effects of the slow-gating ICCD camera.

The following criteria determined the lowest axial positions where signals could be measured. The lowest axial position for the detectable soot PLII signal in C_2H_4 IDFs was where either (a) there was no minimum between the peaks of the PAH PLIF and soot PLII signals or (b) the background signal on the centerline was greater than or equal to the peak soot PLII signal. These conditions were chosen because in case (a), the peak soot PLII signals could not be distinguished from the PAH PLIF, and in case (b), the peak soot PLII could not be distinguished from the centerline background signal. The lowest axial position for the detectable PAH PLIF signal in CH_4 IDFs was defined to be the location at which the peak PLIF PAH signal fell below the sum of the average background signal (165 a.u.) plus three times the standard deviation of the background (35 a.u.). This threshold was chosen because the background signal has a 99.7% probability of being less than this value, assuming a normal distribution. No criterion was required to distinguish the peak PAH PLIF signal in the C_2H_4 IDFs and the peak OH PLIF signals in both flames, because at all axial positions the peak signals were more than three standard deviations greater than the average background signal. The soot PLII signal in CH_4 IDFs was too weak to measure using the laser configuration in this study, and could not be distinguished from the background signals at any axial position.

Radially integrated PAH PLIF and soot PLII signals, $S(z)$, were obtained for each axial position by applying the following formula:

$$S(z) = 2\pi \int_0^R rs(r,z)\mathrm{d}r = 2\pi \sum_{i=1}^{256} r_i s(r_i, z)\Delta r\,, \tag{2}$$

where r and z are the radial and axial positions with respect to the centerline and the top of the burner, R is the radius of the integrated path length (256 pixels = 25.6 mm), $s(r,z)$ is the signal at (r,z), i is the pixel index, and Δr is one pixel width (1 pixel = 0.1 mm). Equation 2 was derived by multiplying the signal strength of the pixel at each radial position by the area of the annulus that passes through the radial position and summing all of the products. Radially integrated signals provide a measure of the total PAH or soot content at each axial position [39-41], but do not necessarily track with the local flux of these entities. The contribution of OH PLIF was deducted before radially integrating PAH PLIF signals.

Temperature Measurements

Radial profiles of temperature were measured in a C_2H_4 IDF with an air flow rate of 1.6 slpm at axial positions of 1.1 cm, 1.5 cm, 2.0 cm, and 2.5 cm. An S-type thermocouple with a wire diameter of 127 μm was used. The thermocouple was welded to an S-type 254 μm diameter thermocouple wire, passed through a ceramic insulator and connected to extension grade thermocouple wire. Thermocouple voltages were amplified with a gain of 207 and recorded on a data acquisition computer at 50 ms intervals. Only twenty data points could be recorded before soot deposition on the thermocouple began to alter the measurements. A micrometer translation stage with 0.01 mm precision was used for radial positioning of the thermocouple bead, and vertical position was obtained with a large translation stage and a millimeter ruler with a precision of 0.5 mm. The thermocouple measurements were corrected for radiation heat loss assuming a cylindrical geometry for the energy balance [42].

Results and Discussion

Flickering in Inverse Diffusion Flames

Figure 3 and Figure 4 show instantaneous images of OH and PAH PLIF and soot PLII from 1.0-slpm and 2.2-slpm air flow rate C_2H_4 IDFs, respectively. The four images in Figure 3 (a) and Figure 4 (a) show OH and PAH PLIF observed with the 340 nm band-pass filter at two instances in time (left and right sides). The four images in Figure 3 (b) and Figure 4 (b) show soot PLII detected with the 570 nm long-pass filter, also at two instances in time (left and right sides). The figures show the degree of buoyancy-induced flickering downstream in the flames. In the 1.0-slpm air flow rate flame, flickering is not very strong near the base of the flame, but downstream it has an observable effect on the PAH layer, with regular vortices forming on both sides of the flame. The soot layer is only affected by flickering in the flow field far downstream from the OH layer. Interestingly, the soot PLII image in Figure 3 (b) shows some PAH PLIF detected with the 570 nm long-pass filter near the base of the flame adjacent to and outside the soot layer. The PAH PLIF and soot PLII signals near the base of the flame appear to have the same magnitude, but they are spatially separated. Unfortunately, it is not possible to detect soot PLII with the present arrangement without also detecting some amount of PAH PLIF. However, at the top of the flame, where the signals overlap, the PAH PLIF signal detected with the 570 nm long-pass filter accounts for less than 10% of the observed soot PLII signal. The vortices observed in the PAH layer in the 2.2-slpm air flow rate IDF shown in Figure 4 (a) are considerably larger than the vortices in the PAH layer in the 1.0-slpm air flow rate IDF shown in Figure 3 (a). The vortices also occur

noticeably lower in the flame in Figure 4 (a) than in Figure 3 (a). Figure 4 (b) shows that the soot layer is also affected by the vortices in the flow field lower in the flame than in Figure 3 (b). It is clear from these images that flickering affects the longer flames in this study more than it affects the shorter flames. Flickering also has a stronger effect on the PAH layers than it has on the OH and soot layers. When average images are presented in the next two sections of this paper, it will be apparent that the flickering has the effect of thickening the mean PAH and soot layers. The IDF flickering observed in Figure 3 and Figure 4 may affect soot formation by increasing the time that soot particles spend at relatively high temperatures near the centerline and transporting growth species such as PAH from cooler regions to hotter regions where soot growth may occur. This is an important concept for use in interpreting the rest of the data provided in this paper.

Structure of Ethylene Inverse Diffusion Flames

Figure 5 depicts images of averaged OH and PAH PLIF from C_2H_4 IDFs detected using the 340 nm band-pass filter. White contours are overlaid to show the locations of peak OH and PAH PLIF and soot PLII signals. In laminar diffusion flames the high temperature reaction zone is tracked by OH radicals [27,28]. The OH layer originates at the top of the burner and is approximately 2 mm thick, which is similar to the thickness of reaction zones in NDFs [27,43]. Compressive strain thickens the OH layer at the flame tip. A high-frequency instability in the 1.4 and 1.6 slpm air flow rate IDFs causes the OH layer to appear thicker than those in the other flames. This instability may also result in enhanced mixing, thereby shortening the mean flames [29]. Originating at the top of the burner, PAH PLIF is present on the outside of the flame in the fuel region.

Near the base of the flame, peak PAH PLIF is observed at increasing radial distance from the central axis as axial distance increases. However, above the top of the reaction zone, at increasing height above the burner, the PAH PLIF signals move closer to the central axis, presumably in response to cool fuel entrainment of the buoyant flame plume. As air flow rate increases from 1.0 slpm to 2.2 slpm, peak PAH PLIF is observed further from the central axis, but never more than 10 mm away. The peak PAH PLIF decreases as air flow rate increases. This may be due to consumption of PAH in soot formation and growth reactions in longer flames that produce more soot, or it may also be because the PAH are more spatially distributed in the longer flames (see Figure 4). Another possibility is that the PAH distribution evolves to larger sizes that are less sensitive to PLIF detection.

Figure 6 depicts averaged images of soot PLII from C_2H_4 IDFs. Soot PLII is present within 2-4 mm of the reaction zone on the fuel side of the flame in between the PAH and OH PLIF, which compares well with the position of soot relative to the reaction zone in many previous studies of both NDFs and IDFs [17,18,26,28,39,44-48]. The soot PLII signal is consistently 2-4 mm away from the PAH layer, which also compares well with previous measurements in both NDFs and IDFs [15,18,26,28,34,41,45,48]. Soot PLII does not originate at the burner exit; instead, it begins about 5 mm from the top of the burner for all flames, independent of the rate of air flow. Qualitatively, the peak soot PLII signal and the apparent width of the soot layer increase with increasing air flow rate. Since the soot layer is not as thick as the PAH layer and does not have the bulges associated with vortices, the time-averaged images confirm that flickering does not appear to affect the soot layer as significantly as it affects the PAH layer.

Depicted in Figure 7 are visible color images of C_2H_4 IDFs with contours of the peak OH and PAH PLIF and soot PLII signals overlaid in white. The blue reaction zone is only visible near the base of the C_2H_4 IDFs. For all air flow rates, luminous soot begins roughly 3 mm from the burner exit, obscures the top of the blue reaction zone, and extends above the peak OH PLIF contour. Luminous soot in the visible color images begins slightly lower than the soot PLII signal, which begins 5 mm above the burner, possibly because smaller soot particles are more difficult to detect by PLII than larger soot particles [31]. The distance of 5 mm from the burner corresponds to a chemical time for soot inception in C_2H_4 IDFs of between 10 ms and 20 ms, assuming a buoyant acceleration of 27 m/s^2 and using the initial air and fuel velocities as the upper and lower bounds. Soot inception time has been previously reported in the range of 10 ms for diffusion flames [49], so the current data are consistent with the literature. The peak soot PLII contour closely follows the outer edge of the luminous soot cone. Signs of flickering are not apparent in the visible images, which is consistent with the low influence of flickering on the soot PLII images, since the visible images consist primarily of soot radiation.

Structure of Methane Inverse Diffusion Flames

Figure 8 depicts images of averaged OH and PAH PLIF in the lower region of CH_4 IDFs detected with the 340 nm band-pass filter. Contours of the peak OH and PAH PLIF signals are overlaid in white. Many features of the CH_4 IDFs are similar to those of C_2H_4 IDFs. The OH layer begins at the burner exit and is about 2 mm thick. The radial location of the peak PAH PLIF decreases with increasing height above the burner. As air

flow rate increases, peak PAH PLIF is observed further from the central axis, but never more than 10 mm away. In the CH_4 IDFs, unlike in the C_2H_4 IDFs, the PAH PLIF does not originate at the burner exit but, instead, is first detected about 10 mm above the top of the burner. Soot PLII could not be measured in CH_4 IDFs using the laser and camera configuration in this study.

Figure 9 depicts visible color images of CH_4 IDFs with contours of peak OH and PAH PLIF overlaid in white. The blue reaction zone is visible for the first 10 millimeters of CH_4 IDFs, although it is dimmer than the blue region in C_2H_4 IDFs. Even though the OH layer begins at the burner exit, the blue reaction zone in CH_4 IDFs is lifted about 1-2 mm above the burner exit. Luminous soot is visible even though soot PLII was not detected (similar to the trend at heights between 3 mm and 5 mm in the C_2H_4 flames). The lack of detectability of soot by PLII could be due to a low soot volume fraction, small soot sizes, and/or the developing optical properties of early soot. Data not shown in Figure 9 indicate that CH_4 IDFs with heights lower than 10 mm do not have visible luminous soot cones [50]. In CH_4 IDFs longer than 10 mm, luminous soot blurs or obscures the tip of the blue reaction zone and extends above the OH PLIF contour. The soot cone is dimmer than the bright yellow soot region in the C_2H_4 IDFs.

Figure 8 and Figure 9 demonstrate that PAH detected at 340 nm in the CH_4 IDFs begin 10 mm above the burner. Although not shown here, PAH detected in the 295-450 nm band begin 5 mm above the burner [50]. The discrepancy between these positions can be attributed to the greater signal-to-noise ratio for PAH PLIF detected with the wider optical band-pass. These PAH starting points can be compared with the visible soot location of 10 mm above the burner. For C_2H_4 flames, PAH detected in both bands

began at the burner surface, while soot formation began 3-5 mm above the burner. Although the relationships between PAH and soot are clearly complex, the data from both fuels show that PAH and soot form sequentially in IDFs, with the bulk PAH formation rate being an important factor in determining when soot appears. While this is similar to known behavior in NDFs, it is significant because the time-temperature histories of soot and its precursors in IDFs may be considerably different from those in NDFs.

PAH PLIF Detection Wavelength Effects

Figure 10 shows a comparison between the peak PAH PLIF position in C_2H_4 IDFs detected with the 340 nm band-pass filter and the 450 nm short-pass filter. Above a height of 20 mm, the PAH PLIF detected with the 450 nm short-pass filter is closer to the reaction zone, occurring in a higher temperature region than PAH PLIF detected at 340 nm. Other researchers have reported that this spectral shift in fluorescence is due to the presence of large aromatics that fluoresce at longer wavelengths and that form at temperatures higher than those at which small aromatics form [28,32,34,45].

Figure 11 shows the peak radially integrated PAH PLIF signals detected with the 450 nm short-pass filter and at 340 nm for both CH_4 and C_2H_4. Peak radially integrated PAH PLIF signals for CH_4 detected with the 450 nm short-pass filter are about 1.3 times the signals detected with the 340 nm band-pass filter [50]. In contrast, peak radially integrated PAH PLIF signals for the C_2H_4 flames in this detection band are three times the signals detected at 340 nm [50]. Since the present CH_4 IDFs produced very little soot and the C_2H_4 IDFs produced more soot, it may be possible that soot production correlates

better with PAH PLIF signals detected with the 450 nm short-pass filter than with PAH PLIF signals detected at 340 nm. This may indicate that the larger, hotter PAH detected with the short-pass filter are more important in soot formation than smaller, cooler PAH detected at 340 nm.

Temperature Effects

Figure 12 contains radial profiles of PLIF detected at 340 nm, PLIF detected between 295 nm and 450 nm, soot PLII, and temperature measurements at three axial positions taken from a C_2H_4 IDF with an air flow rate of 1.6 slpm. Figure 12 (a) contains data from an axial position of 11 mm above the burner. This axial position is below the flame height, so OH PLIF and PAH PLIF are both observed. The OH PLIF peak, which is observed in both PLIF detection bands, coincides with the temperature peak. The soot PLII peak is located where the gas temperature is ~1280 K at 5.1 mm from the centerline. This coincides closely with the lower limit for soot inception (1300 K) cited in numerous other works [51,52]. The fact that soot PLII is observed at temperatures lower than 1300 K (to the right of the soot PLII peak) can be explained by the transport of soot by thermophoresis and momentum, and does not necessarily indicate that the soot formed at this temperature. (Some of the signal to the right of the soot PLII peak can also be attributed to PAH PLIF.) The slope of the radial temperature profile changes slightly on the high temperature side of the soot peak, perhaps due to heat losses from soot radiation. At the edge of the soot peak furthest from the centerline, the temperature profile changes slightly again, perhaps due to convective heat transfer to the surrounding cooler gases. The 295-450 nm PAH PLIF peak is located where the gas temperature is ~830 K at

7.1 mm from the centerline. The 340 nm PAH PLIF peak is located where the gas temperature is ~720 K at 7.5 mm from the centerline.

Figure 12 (b) shows data from an axial position of 15 mm above the burner. The OH PLIF peak and temperature peak are very close to the centerline since this axial position is close to the flame height. The soot PLII peak occurs at a radial distance of 4.7 mm and coincides with a measured temperature of ~1200 K. The same types of changes in the slope of the temperature profile are present at the same relative positions as for the lower flame height. The 295-450 nm PAH PLIF peak is located where the gas temperature is ~870 K at 6.5 mm from the centerline, and the 340 nm PAH PLIF peak is located where the gas temperature is ~670 K at 7.4 mm from the centerline.

Figure 12 (c) shows radial profiles at an axial position of 20 mm. This axial position is above the flame height, so there is no OH PLIF. The soot PLII peak is located at a temperature of ~1190 K at 4.2 mm from the centerline, the 295-450 nm PAH PLIF peak is located at ~980 K at 5.7 mm from the centerline, and the 340 nm PAH PLIF peak is located at ~700 K at 7.1 mm from the centerline. While not shown here, the radial location of the soot PLII peak at a height of 25 mm above the burner is 3.7 mm, corresponding to a measured temperature of ~1070 K [50]. At this height, the 295-450 nm PAH PLIF peak is located at ~970 K at 4.7 mm from the centerline, and the 340 nm PAH PLIF peak is located at ~670 K at 6.6 mm from the centerline.

At all four axial positions, the 295-450 nm PAH PLIF peak is always found where the measured temperature is between 800 K and 1000 K, whereas the 340 nm PAH PLIF peak is always found at a gas temperature of ~700 K. This confirms, in a more quantitative way, the trend observed in Figure 10. In addition, the data show that the

formation of large aromatics, important in soot formation, may require temperatures above 800 K. Below the flame height, the soot PLII peak is found near the minimum soot inception temperature of 1300 K. However, downstream of the flame height, the soot peak is found at lower temperature, even though the soot PLII peak value continues to rise, suggesting that soot growth may occur in IDFs at temperatures below 1300 K. Soot growth at axial temperatures above the flame height where the gas temperature is lower than the soot formation temperature of 1300 K may be due to surface growth reactions and scavenging of PAH.

Residence Time Effects

Figure 13 shows radially integrated PAH PLIF as a function of distance above the burner for C_2H_4 IDFs detected using the 450 nm short-pass filter. Above the OH layer, integrated PAH PLIF increases with axial position for all air flow rates. The 1.0 slpm and 1.2 slpm flames have the lowest integrated PAH signals, consistent with their short flame heights. The longer flames with air flow rates of 1.4 slpm and above have relatively greater integrated PAH signals. Above 50 mm, the integrated signals for some of the air flow rates appear to plateau and decrease, which may due to scavenging of PAH by soot, the contraction and acceleration of the PAH layer, or a reduced fluorescence sensitivity associated with changes in the PAH size distribution or temperature. The decrease in signals above 65 mm may also be due to the irising effect of the camera. Interestingly, the decrease in PAH signal above 50 mm was not observed in the PAH PLIF signals detected with the 340 nm band-pass filter [50], perhaps

supporting the observation that the small PAH detected in that band were less influential in soot formation.

Radially integrated soot PLII from C_2H_4 IDFs is shown in Figure 14. Integrated signals increase until the top of the high temperature reaction zone, after which the slopes of the signals gradually decrease. This may indicate that soot inception has ceased, and the integrated soot PLII signal is increasing due to soot growth. High in the flames, at about 45 mm above the burner, the integrated signals approach constant values, as soot formation and growth mechanisms become frozen. This trend agrees well with the leveling off of radially integrated IDF soot concentration data reported by Makel and Kennedy [39].

Figure 15 shows the maximum radially integrated soot PLII signal as a function of the rate of air flow in C_2H_4 IDFs. The maximum integrated soot signal increases linearly with increasing air flow rate. Since, in buoyant IDFs, flame height and residence time are determined by air flow rate [29,53], Figure 15 indicates that the amount of soot produced increases with flame residence time and is directly proportional to flame height. Extrapolation of Figure 15 also predicts that an ethylene IDF with an air flow rate less than 0.6 slpm will produce no soot.

Figure 16 shows radially integrated PAH PLIF detected with the 450 nm short-pass filter in CH_4 IDFs. Radially integrated PAH PLIF above the OH layer increases monotonically for all air flow rates instead of leveling off like the C_2H_4 PAH PLIF signals, presumably because PAH are not scavenged by soot in the CH_4 flames.

Conclusions

Flame structure of C_2H_4 IDFs and CH_4 IDFs was studied using simultaneous OH and PAH PLIF, soot PLII, and selected thermocouple measurements. Several IDFs of different air flow rates were studied for each fuel type. The measurements provide insight on the IDF structure and the role of PAH in soot formation in IDFs and underventilated combustion. Soot growth seems to occur in IDFs from reactions with large PAH close to the soot layer at temperatures below 1200 K – 1300 K, considered to be the minimum soot inception temperature.

It was observed that the distances between the OH, PAH and soot zones are similar in IDFs and NDFs, but the locations of those zones are inverted in IDFs relative to NDFs.Peak OH PLIF occurred just inside the outer boundary of the blue emission in visible images of both C_2H_4 and CH_4 IDFs and coincided with peak temperature measured in a C_2H_4 IDF, which indicates that OH PLIF can be used to locate the reaction zone in laminar IDFs. PAH formation either preceded or was coincident with the axial location where soot appeared. This suggests that PAH may be a constituent in soot formation in IDFs and that its formation may be a rate-limiting step in soot formation in IDFs. While this is similar to known soot behavior in NDFs, it is significant because the time-temperature histories of soot and its precursors in IDFs may be considerably different from those in NDFs.

In C_2H_4 IDFs, the location of peak PAH PLIF coincided with measured temperatures of 800 K to 1000 K for the long wavelength detection band and 700 K for the shorter wavelength detection band, which may also indicate the minimum critical temperature, 800 K, above which these large aromatics will form. The location of peak

soot PLII near the reaction zone coincided with a measured temperature between 1200 K and 1300 K in a C_2H_4 IDF, which corresponds to the critical soot inception temperature reported for NDFs. This indicates that the soot formation mechanisms in IDFs and NDFs are similar. Measured temperatures along the peak soot PLII contour decreased with increasing distance above the flame height, even though radially integrated soot PLII continued to increase. This suggests that soot growth can occur at temperatures below the soot inception temperature, probably by scavenging PAH.

Radially integrated soot PLII increased with axial position below the flame height. Above the flame height, it increased with a lower slope, reaching a maximum constant value at a point downstream of the reaction zone. This suggests that soot inception ceased above the reaction zone and that only soot growth was occurring immediately after the reaction zone until further downstream where all soot chemistry froze.

Acknowledgments

This research was funded by the NASA microgravity combustion program under multiple contracts and by the Strategic Environmental Research and Development Program. Sandia is a multiprogram laboratory operated by the Sandia Corporation, a Lockheed Martin Company, for the United States Department of Energy's National Nuclear Security Administration under Contract DE-AC04-94AL85000. Additional support was provided by a Laboratory Directed Research and Development project at Sandia National Labs.

References

[1]. J.S. Lighty, J.M. Veranth, A.F. Sarofim, Journal of the Air and Waste Management Association 50 (9) (2000) 1565-1618.

[2]. K.M. Butler, G.W. Mulholland, Fire Technology 40 (2) (2004) 149-176.

[3]. B.S. Haynes, H.Gg. Wagner, Prog. Energy Combust. Sci. 7 (4) (1981) 229-273.

[4]. C.W. Lautenberger, J.L. de Ris, N.A. Dembsey, J.R. Barnett, H.R. Baum, Fire Safety Journal 40 (2) (2005) 141-176.

[5]. J.L. De Ris, P.K. Wu, G. Heskestad, Proc. Combust. Inst. 28 (2000) 2751-2758.

[6]. J.L. De Ris, Proc. Combust. Inst. 17 (1978) 1003-1015.

[7]. R.L. Schalla, G.E. McDonald, Proc. Combust. Inst. 5 (1955) 316-324.

[8]. I. Glassman, Proc. Combust. Inst. 22 (1988) 295-311.

[9]. I.M. Kennedy, Prog. Energy Combust. Sci. 23 (2) (1997) 95-132.

[10]. A. D'anna, A. D'alessio, J. Kent, Combust. Sci. Technol. 174 (11-2) (2002) 279-294.

[11]. M. Frenklach, Physical Chemistry Chemical Physics 4 (11) (2002) 2028-2037.

[12]. F. Liu, H.S. Guo, G.J. Smallwood, O.L. Gulder, Combustion Theory and Modelling 7 (2) (2003) 301-315.

[13]. S. Leonard , G.W. Mulholland, R. Puri, R.J. Santoro, Combust. Flame 98 (1-2) (1994) 20-34.

[14]. K.T. Wu, R.H. Essenhigh, Proc. Combust. Inst. 20 (1984) 1925-1932.

[15]. K.T. Kang, J.Y. Hwang, S.H. Chung, W. Lee, Combust. Flame 109 (1-2) (1997) 266-281.

[16]. G.W. Sidebotham, I. Glassman , Combust. Flame 90 (3-4) (1992) 269-283.

[17]. J.H. Kent, H.G. Wagner, Zeitschrift Fur Physikalische Chemie-Wiesbaden 139 (1984) 59-68.

[18]. C.R. Shaddix, C.W. Williams, L.G. Blevins, R.W. Schefer, Proc. Combust. Inst. 30 (2005) 1501-1508.

[19]. J.R. Arthur, B.T. Commins, A.S. Gilbert, A.J. Lindsey, D.H. Napier, Combust.

Flame 2 (1958) 267-272.

[20]. A. Tewarson, J. Steciak, Combust. Flame 53 (1-3) (1983) 123-134.

[21]. G.W. Sidebotham, I. Glassman , Combust. Sci. Technol. 81 (4-6) (1992) 207-219.

[22]. J.R. Arthur, D.H. Napier, Proc. Combust. Inst. 5 (1955) 303-316.

[23]. J.R. Arthur, P.K. Kapur, D.H. Napier, Nature 169 (1952) 372-373.

[24]. L.G. Blevins, R.A. Fletcher, B.A. Benner, E.B. Steel, G.W. Mulholland, Proc. Combust. Inst. 29 (2003) 2325-2333.

[25]. A. Santamaria, F. Mondragon, A. Molina, N.D. Marsh, E.G. Eddings, A.F. Sarofim, Combust. Flame 146 (1-2) (2006) 52-62.

[26]. E.J. Lee, K.C. Oh, H.D. Shin , Fuel 84 (5) (2005) 543-550.

[27]. K.C. Smyth, P.J.H. Tjossem, A. Hamins, J.H. Miller, Combust. Flame 79 (3-4) (1990) 366-380.

[28]. K.C. Smyth, J.H. Miller, R.C. Dorfman, W.G. Mallard, R.J. Santoro, Combust. Flame 62 (2) (1985) 157-181.

[29]. M.A. Mikofski, T.C. Williams, C.R. Shaddix, L.G. Blevins, Combust. Flame 146 (1-2) (2006) 63-72.

[30]. S.R. Turns, An Introduction to Combustion: Concepts and Applications, McGraw-Hill, Boston, 2000, p. 656.

[31]. C.R. Shaddix, K.C. Smyth, Combust. Flame 107 (4) (1996) 418-452.

[32]. J.H. Miller, W.G. Mallard, K.C. Smyth, Combust. Flame 47 (1982) 205-214.

[33]. A. Leipertz, F. Ossler, M. Aldén, in: K. Kohse-Höinghaus, J.B. Jeffries (Eds.), Applied Combustion Diagnostics, Taylor & Francis, New York, 2002, p. 359.

[34]. R.L. Vanderwal, K.A. Jensen, M.Y. Choi, Combust. Flame 109 (3) (1997) 399-414.

[35]. F. Ossler, T. Metz, M. Alden , Applied Physics B-Lasers and Optics 72 (4) (2001) 465-478.

[36]. A.C. Eckbreth, J. Appl. Phys. 48 (11) (1977) 4473-4479.

[37]. R.J. Santoro, Shaddix C.R., in: K. Kohse-Höinghaus, J.B. Jeffries (Eds.), Applied Combustion Diagnostics, Taylor & Francis, New York, 2002, p. 252.

[38]. D.R. Snelling, F. Liu, G.J. Smallwood, O.L. Gulder, Combust. Flame 136 (1-2) (2004) 180-190.

[39]. D.B. Makel , I.M. Kennedy, Combust. Sci. Technol. 97 (4-6) (1994) 303-314.

[40]. F.G. Roper, C. Smith, Combust. Flame 36 (1979) 125-138.

[41]. R.J. Santoro, H.G. Semerjian, R.A. Dobbins, Combust. Flame 51 (2) (1983) 203-218.

[42]. C.R. Shaddix, in: Proceedings of the 33rd National Heat Transfer Conference, ASME, New York, 1999,

[43]. R.E. Mitchell, A.F. Sarofim, L.A. Clomburg, Combust. Flame 37 (3) (1980) 227-244.

[44]. J.H. Kent, H.G. Wagner, Combust. Flame 47 (1) (1982) 53-65.

[45]. G. Prado, A. Garo, A. Ko, A.F. Sarofim, Proc. Combust. Inst. 20 (1984) 989-996.

[46]. C. Wey, E.A. Powell, J.I. Jagoda, 20 (1984) 1017-1024.

[47]. R.J. Santoro, T.T. Yeh, J.J. Horvath, H.G. Semerjian, Combust. Sci. Technol. 53 (2-3) (1987) 89-115.

[48]. K.C. Smyth, C.R. Shaddix, D.A. Everest, Combust. Flame 111 (3) (1997) 185-207.

[49]. A. Thomas, Combust. Flame 6 (1962) 46-62.

[50]. M.A. Mikofski, Ph.D. dissertation, University of California, Berkeley, 2005.

[51]. J. Du, R.L. Axelbaum, Combust. Flame 100 (3) (1995) 367-375.

[52]. R.A. Dobbins, Combust. Flame 130 (3) (2002) 204-214.

[53]. F.G. Roper, Combust. Flame 29 (1977) 219-226.

List of Tables

List of Figures

Table 1: Flow Conditions.

Fuel	Q_{fuel}[a]	Q_{air}[b]	V_{fuel}[c]	V_{air}[d]	V_{air}/V_{fuel}	$Re_{fuel,Dc}$[e]	$Re_{air,Dair}$[f]	Fr[g]	$\Phi_{overall}$[h]	HRR_{air}[i]
	slpm	slpm	cm/s	cm/s						W
CH_4	3.8	1.2	10	26	2.5	120	170	0.19	30	70
		1.3		28	2.7		180	0.20	28	76
		1.6		34	3.3		230	0.35	23	93
		1.7		36	3.5		240	0.34	22	99
		1.8		38	3.8		250	0.35	20	110
		2.0		42	4.2		280	0.37	18	120
		2.2		47	4.6		310	0.39	17	130
		2.4		51	5.0		340	0.42	15	140
		2.6		55	5.4		370	0.44	14	150
		2.7		57	5.6		380	0.45	14	160
C_2H_4	2.7	1.0	7.2	21	2.9	170	140	0.18	39	64
		1.2		26	3.5		170	0.19	32	77
		1.4		30	4.1		200	0.21	28	90
		1.6		34	4.8		230	0.32	24	100
		1.8		38	5.3		250	0.33	22	120
		2.0		42	5.9		280	0.35	19	130
		2.2		47	6.5		310	0.38	18	140

[a] Q_{fuel}, volume flow rate of fuel (at 293 K and 101 kPa).

[b] Q_{air}, volume flow rate of air (at 293 K and 101 kPa).

[c] V_{fuel}, average cold-flow fuel velocity at the burner exit.

[d] V_{air}, average cold-flow air velocity at the burner exit.

[e] $Re_{fuel,Dc}$, Reynolds number based on the cold-flow conditions of the fuel at the burner exit and the hydraulic diameter, D_c = 2 cm.

[f] $Re_{air,Dair}$, Reynolds number based on the cold-flow conditions of the air at the burner exit and the air tube diameter, D_{air} = 1 cm.

[g] Fr, Froude number, defined according to Ref. [30].

[h] $\Phi_{overall}$, overall equivalence ratio, defined as the fuel-to-air ratio divided by the stoichiometric fuel-to-air ratio.

[i] HRR_{air}, the estimated heat release rate based on the heating value of the fuel assuming all of the air reacts completely.

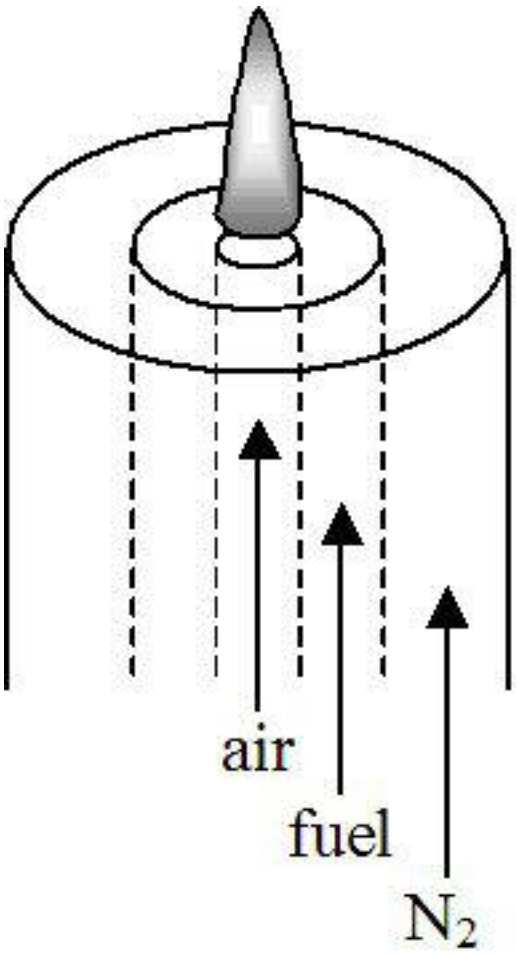

Figure 1: Schematic diagram of burner.

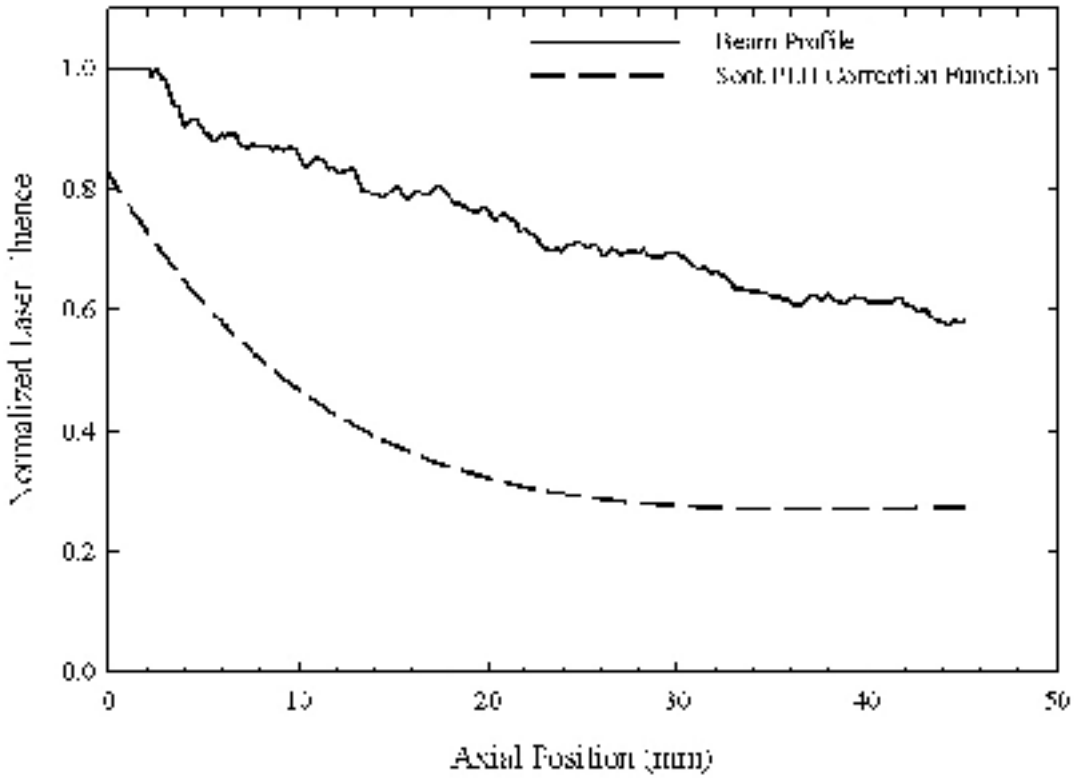

Figure 2: Spatial variation in the laser beam profile, measured from Rayleigh scattering through room temperature air, and soot PLII correction function, both normalized by maximum laser fluence.

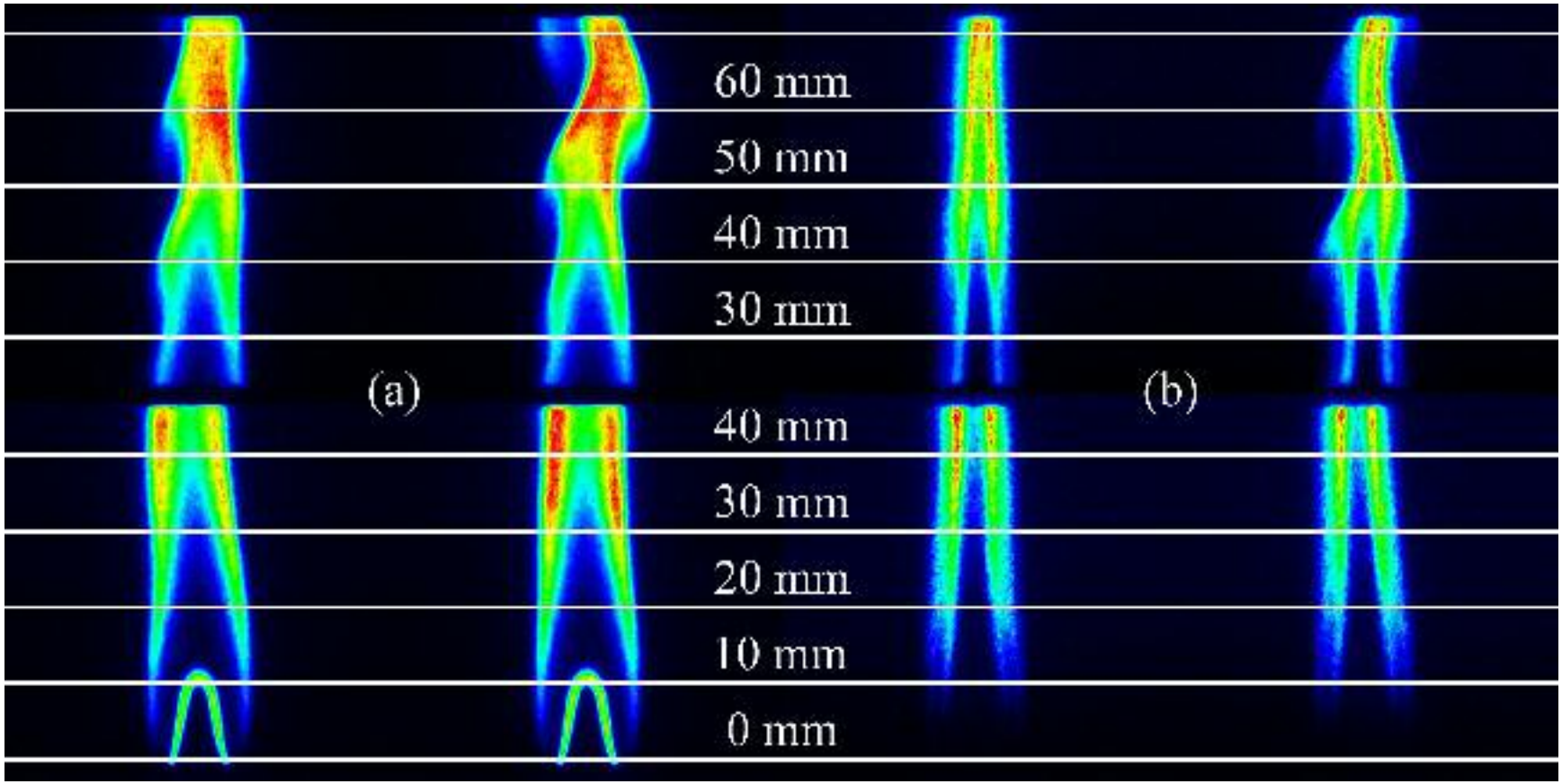

Figure 3: Two instantaneous images of 1.0-slpm air flow rate ethylene IDF. (a) OH and PAH PLIF detected with 340 nm band-pass filter. (b) Soot PLII. The top figures show images of the flames from 23 mm to 74 mm above the burner, and the bottom figures show images of the flames from the 0 mm to 48 mm above the burner.

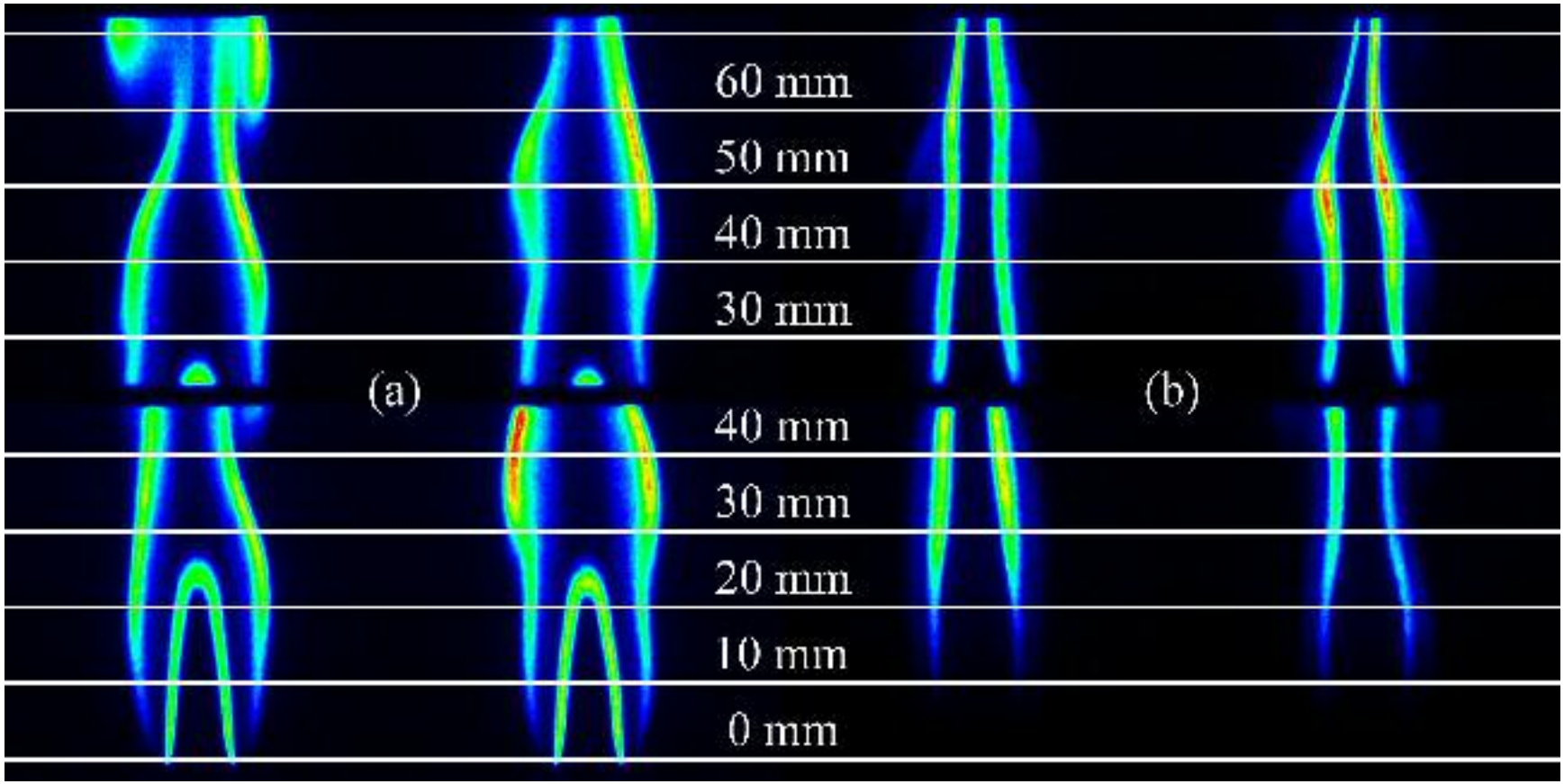

Figure 4: Two instantaneous images of 2.2-slpm air flow rate ethylene IDF. (a) OH and PAH PLIF detected with 340 nm band-pass filter. (b) Soot PLII. The top figures show images of the flames from 23 mm to 74 mm above the burner, and the bottom figures show images of the flames from the 0 mm to 48 mm above the burner.

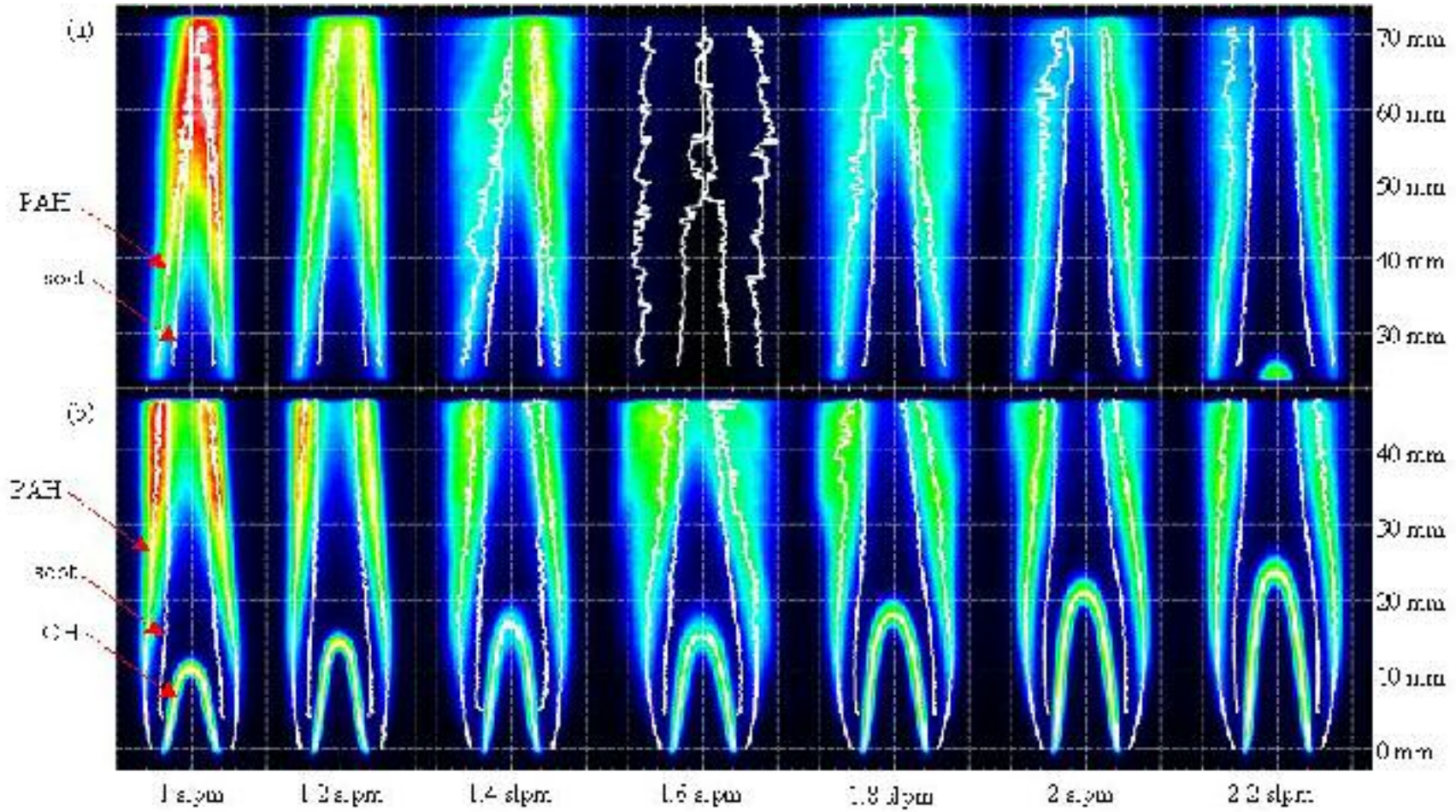

Figure 5: Color-maps of time-averaged OH and PAH PLIF detected with 340 nm band-pass filter from ethylene IDFs of varying air flow rates with contours of peak PLIF and PLII overlaid in white. (a) PAH PLIF from 23 mm to 74 mm above burner with intensity divided by a scaling factor of 13440. The signal for the 1.62 slpm air flow rate IDF is low because the laser was blocked. (b) PAH and OH PLIF from 0 mm to 48 mm above burner with intensity divided by a scaling factor of 10000. The intensity of the PLIF signals is color-mapped such that black, blue, green, red, and white represent increasing intensity, respectively.

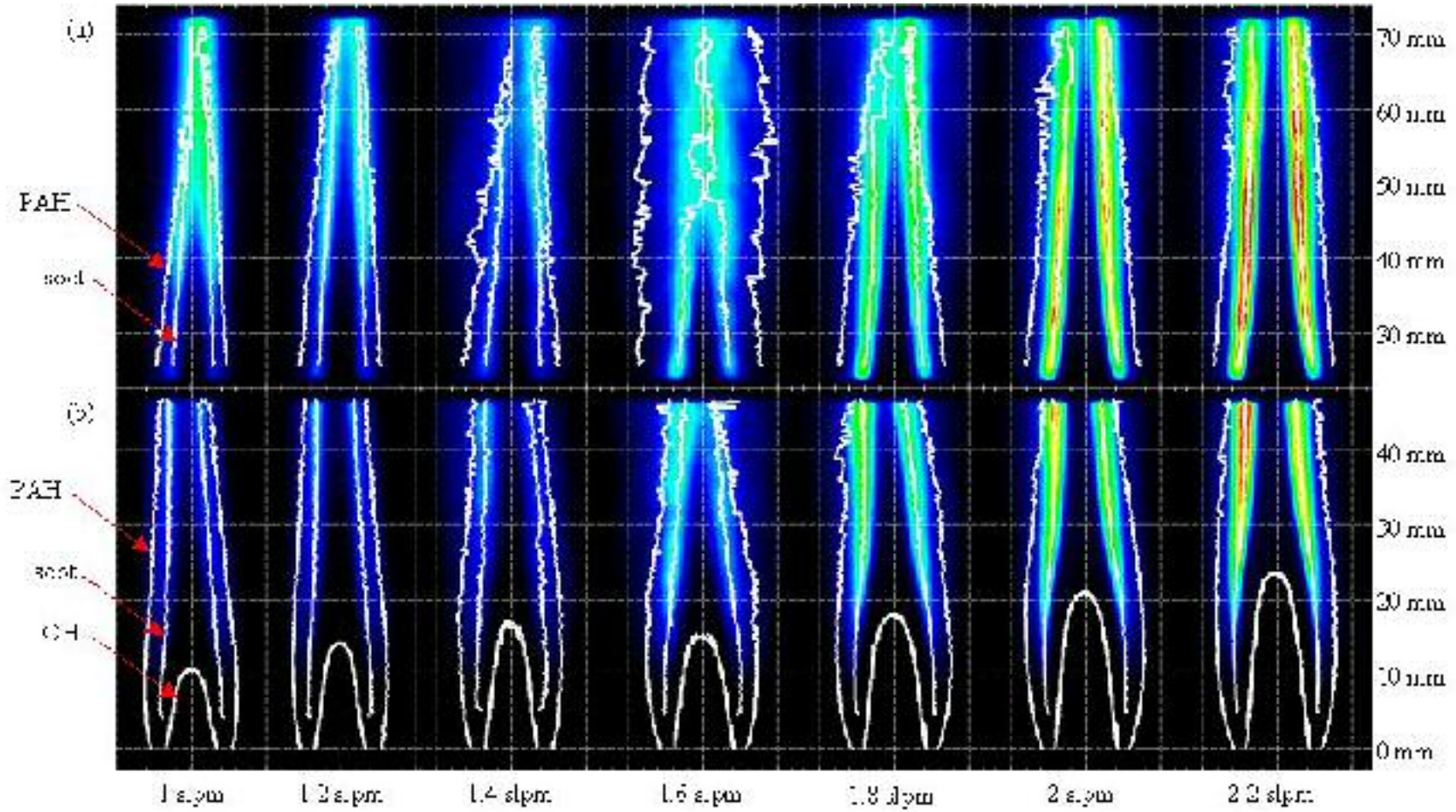

Figure 6: Color-maps of time-averaged soot PLII from ethylene IDFs of varying air flow rates with contours of peak PLIF and PLII overlaid in white. (a) Soot PLII from 23 mm to 74 mm above burner with intensity divided by a scaling factor of 33907. (b) Soot PLII from 0 mm to 48 mm above burner with intensity divided by a scaling factor of 37450. The intensity of the PLII signals is color-mapped such that black, blue, green, red, and white represent increasing intensity, respectively.

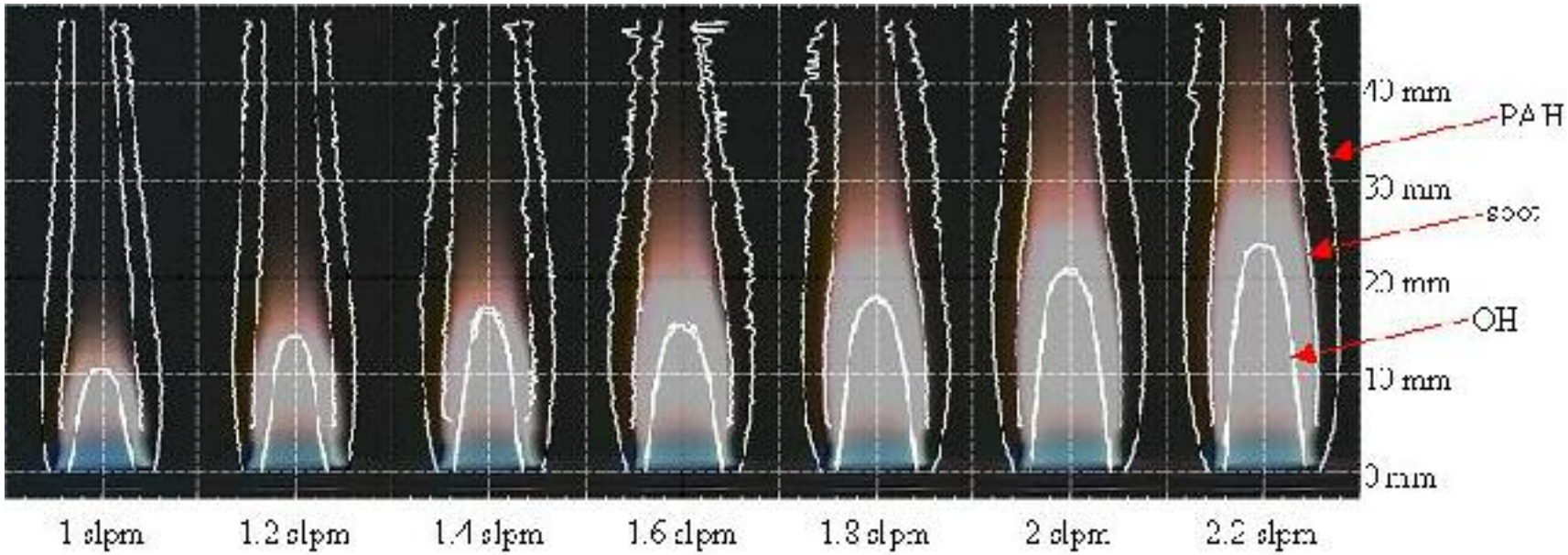

Figure 7: Visible color images of ethylene-air IDFs with contours of the peak time-averaged PLIF and PLII signals overlaid.

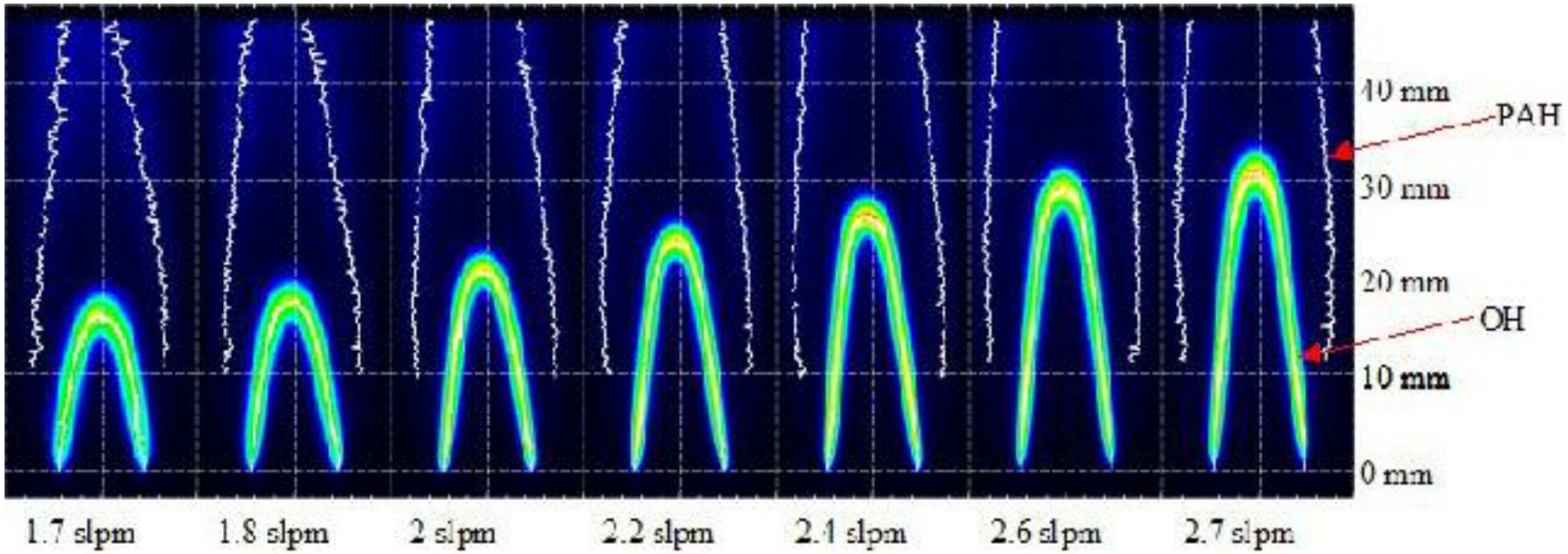

Figure 8: Color-maps of time-averaged OH and PAH PLIF detected with 340 nm band-pass filter from methane IDFs of varying air flow rates with contours of peak PLIF overlaid in white. The intensity of the PLIF signals is divided by a scaling factor of 6200 and color-mapped such that black, blue, green, red, and white represent increasing intensity, respectively.

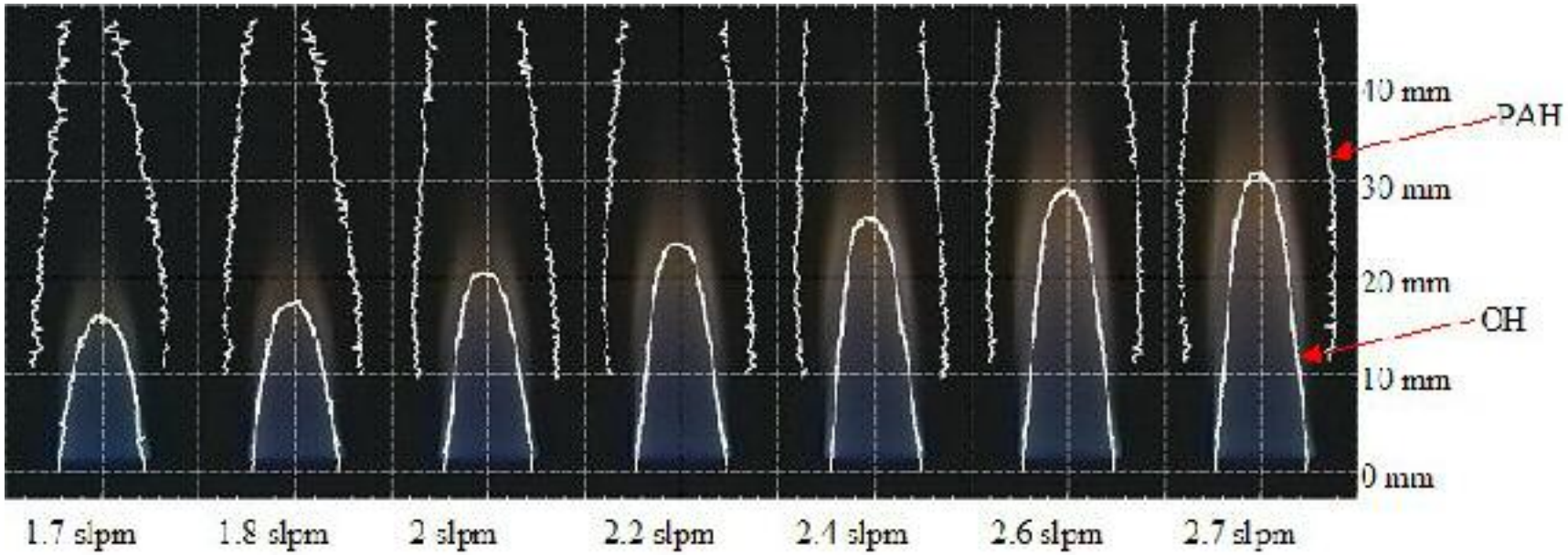

Figure 9: Visible color images of methane-air IDFs with contours of the peak time-averaged PLIF signals overlaid.

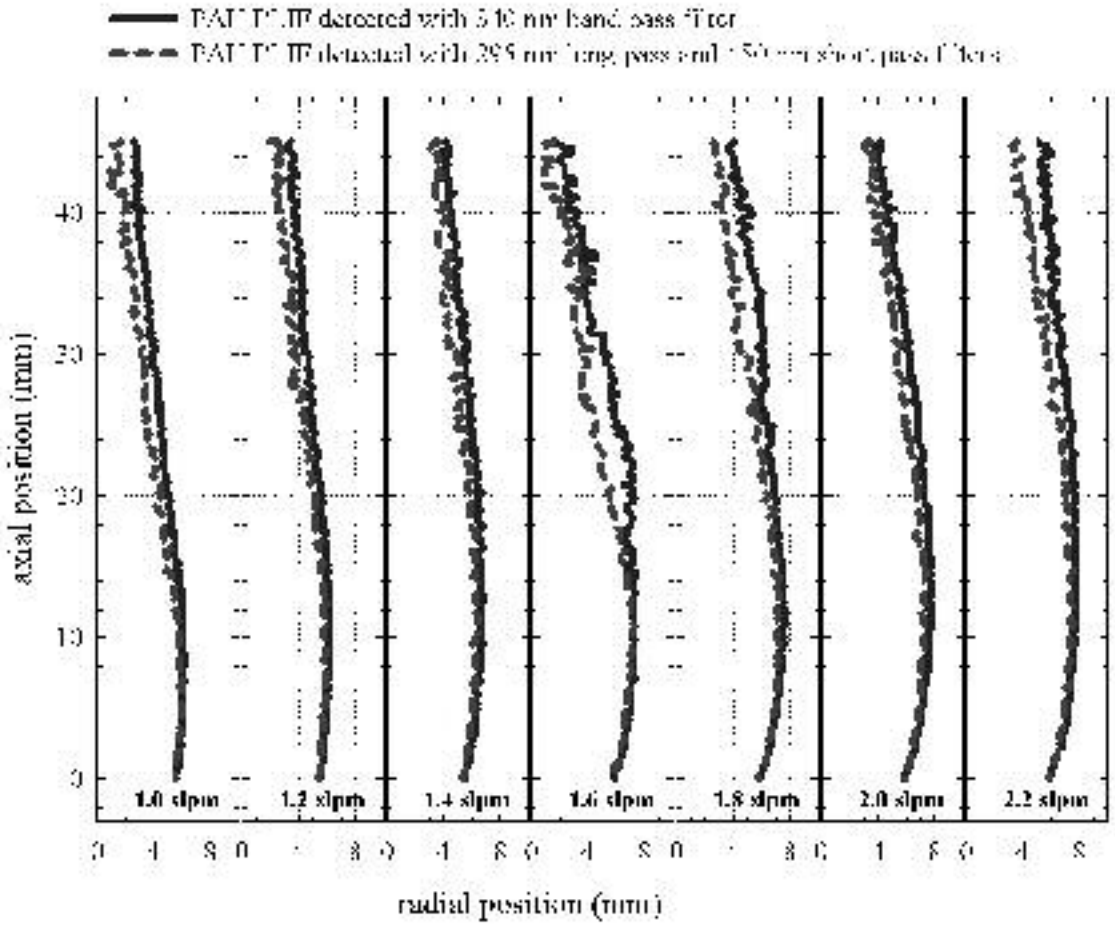

Figure 10: Comparison between the peak PAH PLIF position detected with a 340 nm band-pass filter and detected with a 450 nm short-pass filter in ethylene IDFs of varying air flow rates. Only the right side of the flames are shown.

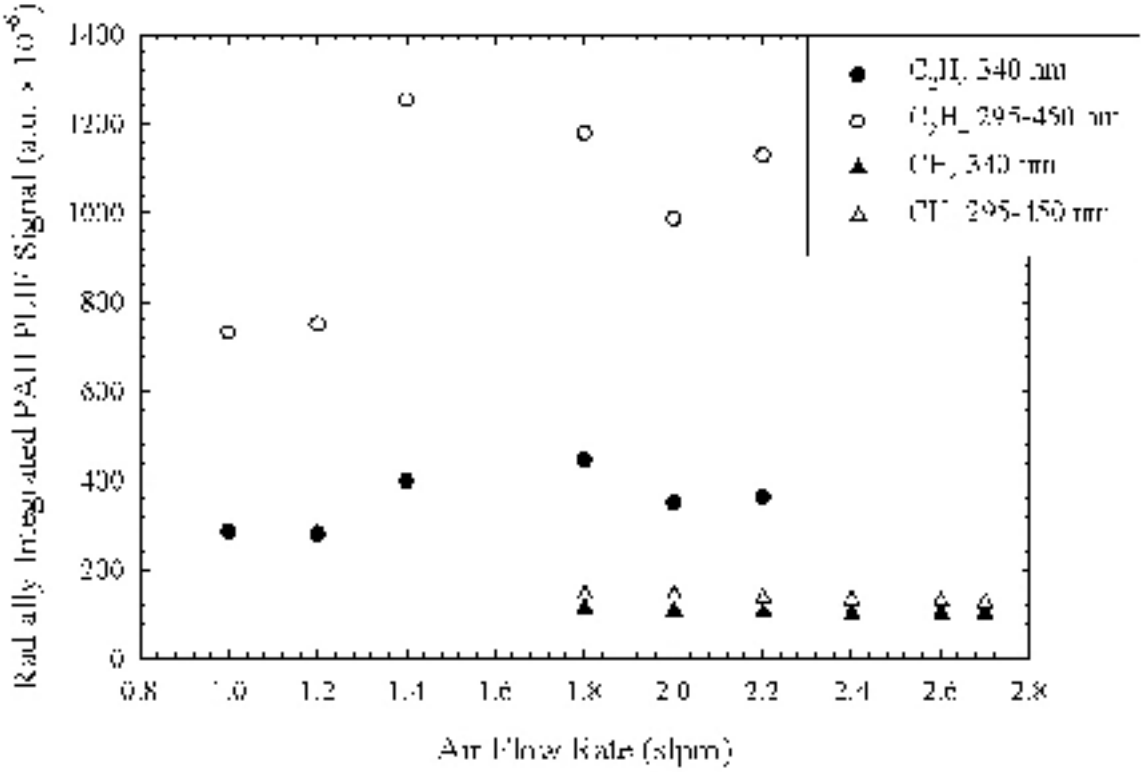

Figure 11: Peak radially integrated PAH PLIF as a function of air flow rate for all methane and ethylene IDFs detected in two wavelength bands.

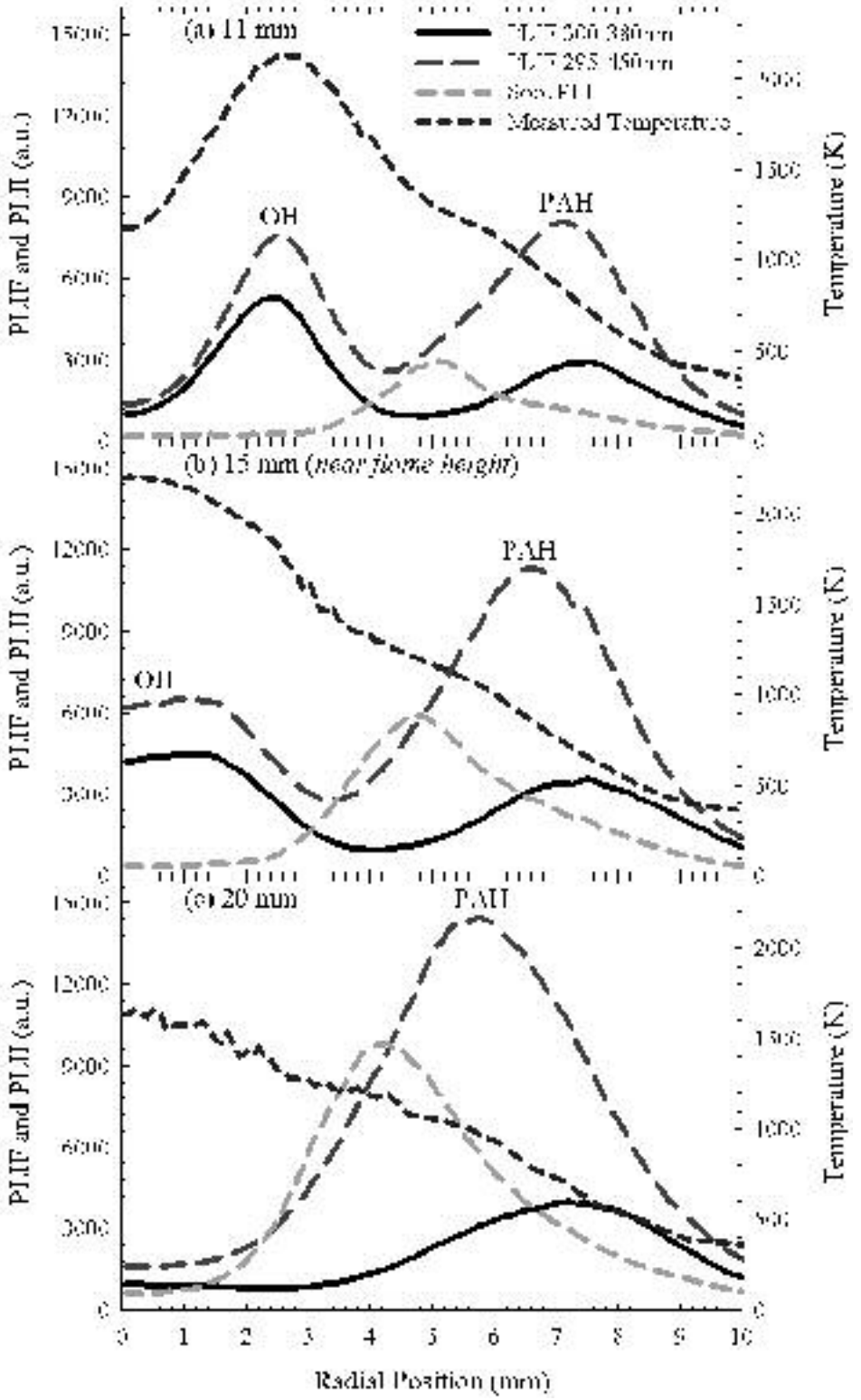

Figure 12: Radial profiles of PLIF detected with 340 nm band-pass filter, PLIF detected with a 450 nm short-pass filter, soot PLII, and temperature measurements in a 1.6 slpm air flow rate ethylene IDF at axial positions of (a) 11 mm, (b) 15 mm, and (c) 20 mm.

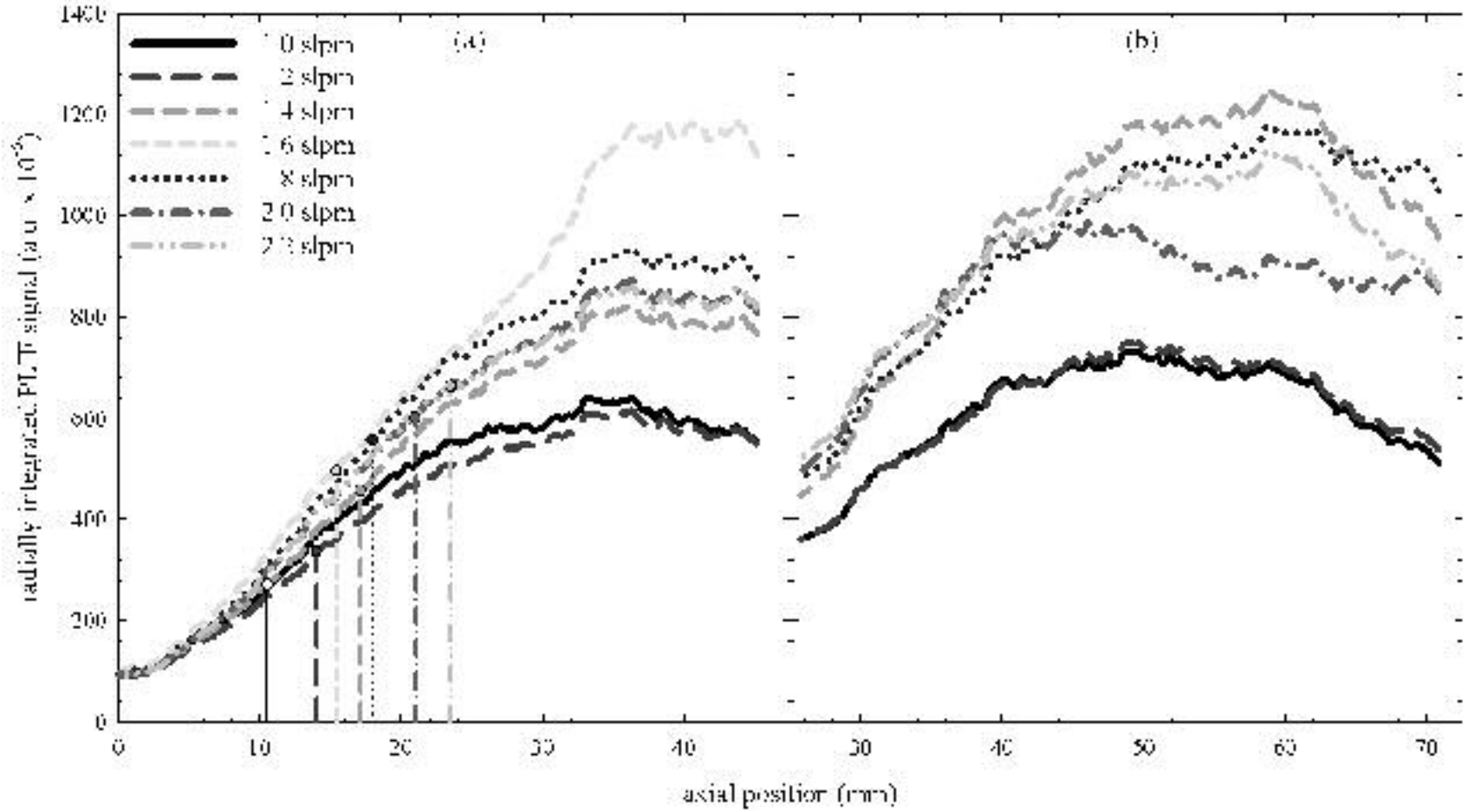

Figure 13: Radially integrated PAH PLIF detected with a 450 nm short-pass filter in ethylene IDFs versus axial position from 0 mm to 45 mm (a), and from 26 mm to 71 mm (b) above the burner. Drop down lines indicate stoichiometric flame height.

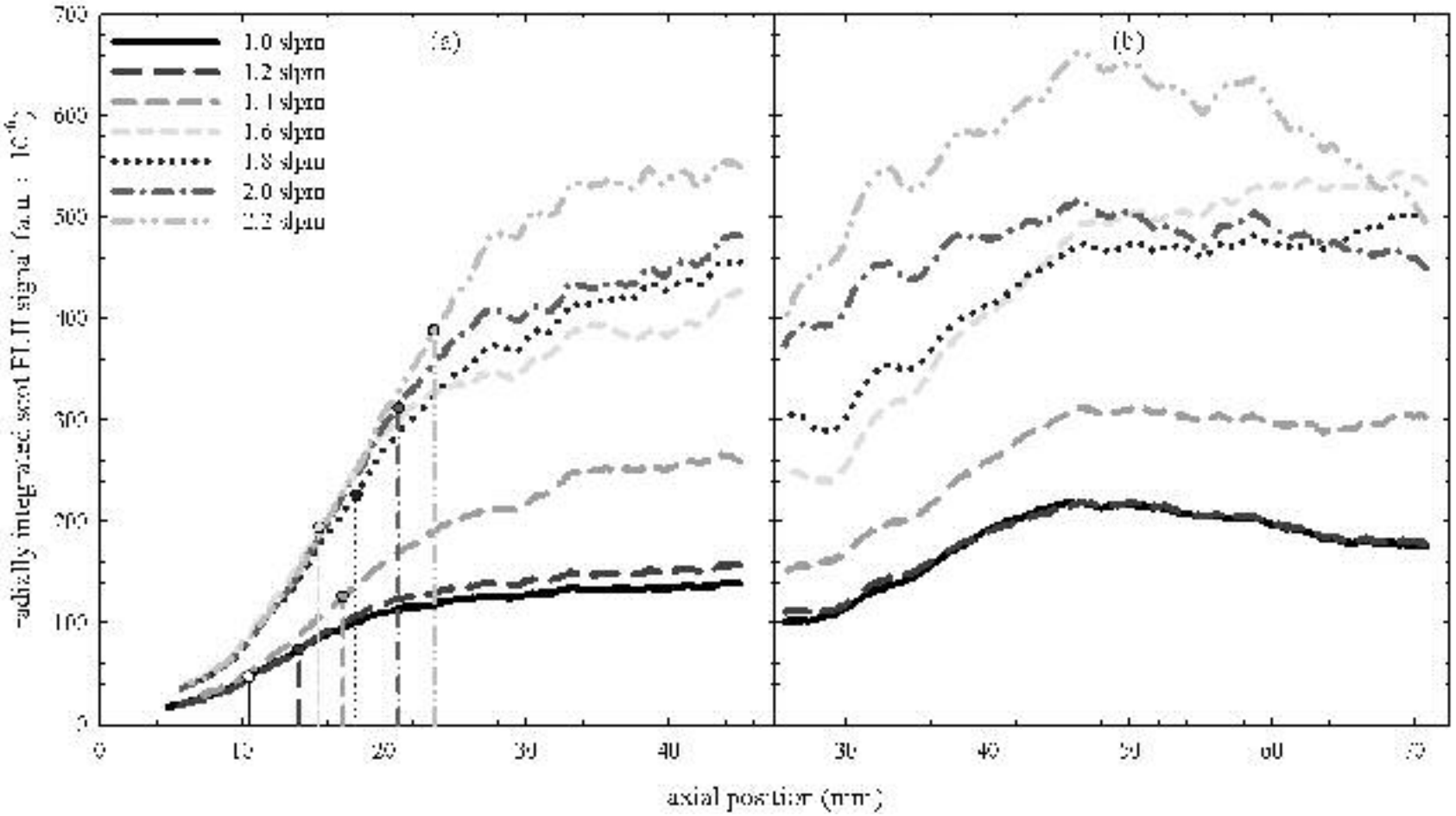

Figure 14: Radially integrated soot PLII in ethylene IDFs versus axial position from 0 mm to 45 mm (a), and from 26 mm to 71 mm (b) above the burner. Drop down lines indicate stoichiometric flame height.

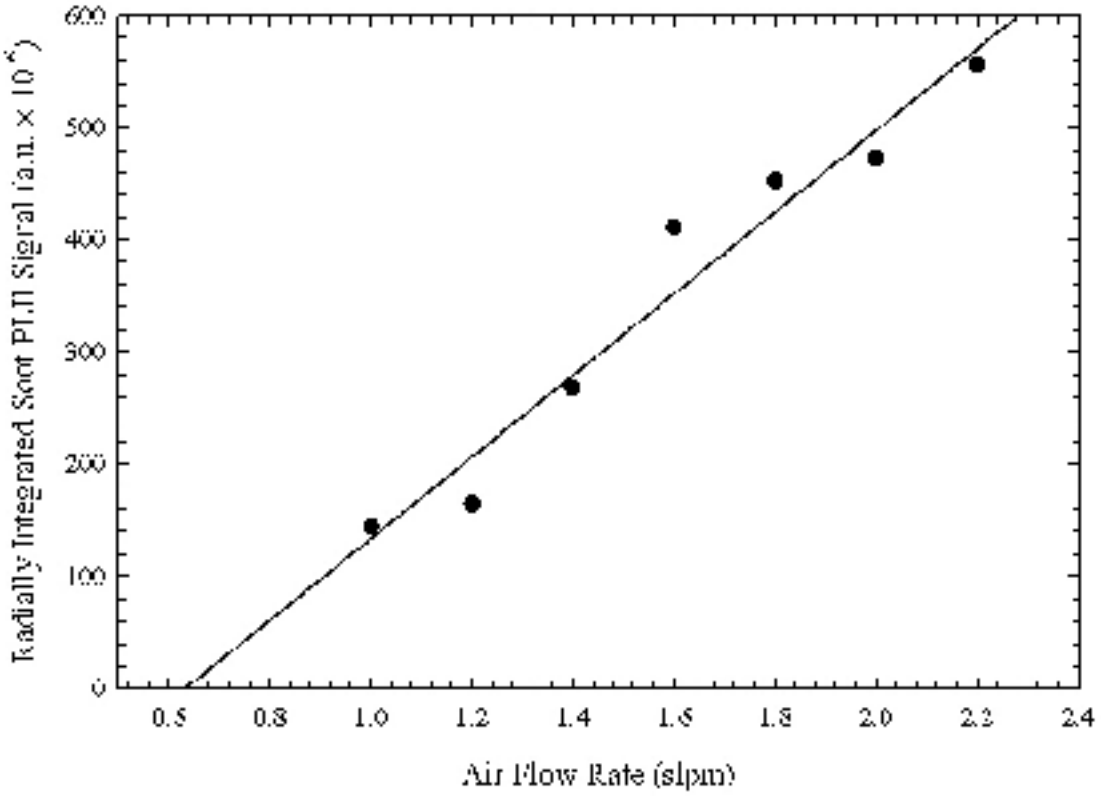

Figure 15: Maximum radially integrated soot PLII signal versus air flow rate for ethylene IDFs.

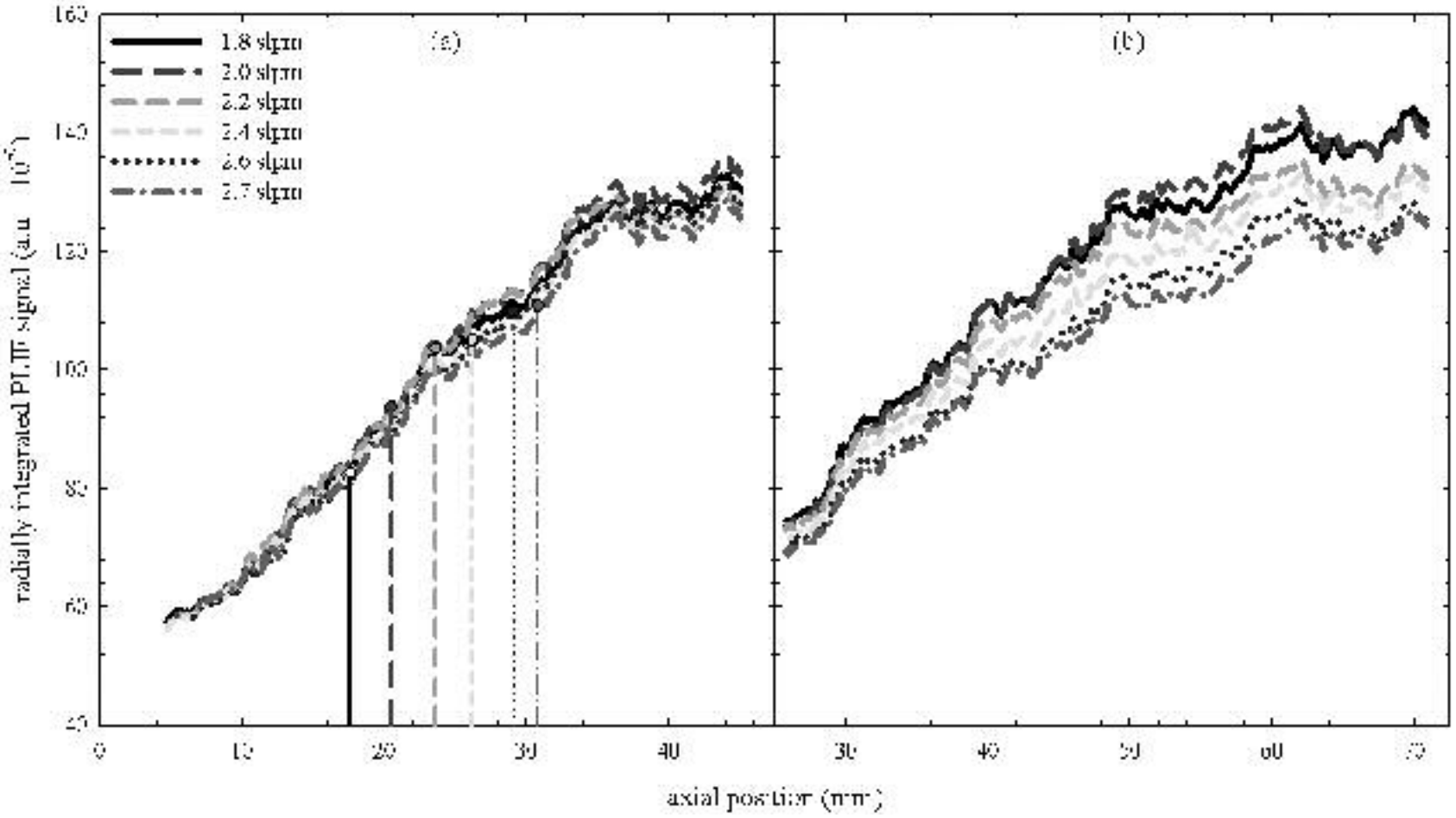

Figure 16: Radially integrated PAH PLIF detected with a 450 nm short-pass filter in methane IDFs versus axial position from 0 mm to 45 mm (a), and from 26 mm to 71 mm (b) above the burner. Drop down lines indicate stoichiometric flame height.